

## LOW LEVEL RF SYSTEM FOR STAR THOMSON SCATTERING SOURCE

L. Piersanti<sup>1</sup>, P. Baldini<sup>1</sup>, M. Bellaveglia<sup>1</sup>, A. Gallo<sup>1</sup>,  
S. Quaglia<sup>1</sup>, M. Scampati<sup>1</sup>, A. Spreccaceneri<sup>1</sup>

<sup>1)</sup> *INFN, Laboratori Nazionali di Frascati, P.O. Box 13, I-00044 Frascati, Italy*

April 8, 2019

### Abstract

STAR project (Southern european Thomson source for Applied Research) foresees the construction of an advanced Thomson source at the UNICAL campus in Rende (CS, Italy) by a collaboration made of several research institutes and Universities, such as: UniCal, CNISM, INFN and Sincrotrone Trieste. Monochromatic, ps-long, polarized X-ray beams will be produced with tunable energy between 20 and 140 keV by means of S-band (2856 MHz) electron photo-injector. This is composed of a Standing Wave (SW) RF-gun and a 3 meter long SLAC-type Traveling Wave (TW) section combined with 100 Hz 5 ps 130 mJ laser system. In this document we will review the complete low level RF system, custom made by INFN-LNF RF group. This system includes three main blocks: (i) the splitting board that amplifies the RF reference for the demodulation and the distribution to the various clients; (ii) the distribution board required for the RF-gun, the TW section, the photocathode laser and the interaction laser; (iii) a 8 channels direct conversion receiver. The system also includes the power supply for the splitting board, and the power amplifier that drives the klystron RF pulse, which have been both tested by INFN-LNF RF group but purchased by STAR collaboration.

PACS:

## Introduction

Nowadays Thomson scattering X-ray sources represent a flexible, compact and cost effective solution with respect to standard synchrotron light sources. Several projects worldwide are adopting such production scheme [1, 2, 3] for applications that range from medical science and biology to material science.

Thomson scattering is the electromagnetic process where an electron absorbs one or more photons from a laser source and emits one photon. If the electrons are relativistic, the radiation is Doppler shifted at higher frequencies (at small angles  $\nu' \simeq 4\gamma^2\nu$ ) and it is emitted in forward direction (with respect to the electron beam) with a small aperture angle proportional to the inverse of Lorentz relativistic factor  $\gamma$ .

The STAR facility will be built, commissioned and operated at UniCal campus in Rende (CS, Italy) in a new building designed to host the accelerator, the laser clean room and the experimental hall. The electrons will be accelerated by means of a S-band photo-injector: a 1.6 Cell RF-gun followed by one SLAC-type 3 m long TW accelerating section. The use of a solenoid after the RF-gun together with the TW section will provide the required emittance compensation [4], scheme which has been studied and tested at SPARC\_LAB [5, 6] and has already been adopted in several laboratories worldwide. The electron bunches (accelerated up to an energy of 60 MeV) will be delivered to the interaction point (IP) where a Yb:YAG 100 Hz high quality laser has to be synchronized to the RF system and to the photocathode laser with a relative time jitter lower than 1 ps.

The S-band low level RF (LLRF hereafter) system realized for STAR project and presented in this technical note represents the result of the experience acquired by the INFN-LNF RF group during the design, test, installation and commissioning phases of the SPARC\_LAB LLRF. In fact, both systems are based on a similar architecture, work at the same frequency and share the direct conversion approach with I/Q demodulation. Nevertheless, a dedicated algorithm for amplitude and phase calculation, that takes into account the imbalance of different I/Q mixers, has been developed specifically for STAR project. This will be presented in the following sections together with the RF measurements and the achieved performance of the entire system.

## 1 Low level RF system

The LLRF system for STAR project, whose block diagram is shown in Figure 1, has been developed and tested at INFN-LNF and it comprises three sub-systems: (i) a splitting board that amplifies the RF reference to the desired level needed for the demodulation and for the distribution to the clients; (ii) a distribution board consisting of three delay lines, a variable attenuator and a RF switch required for the RF-gun, the TW section, the photocathode laser and the interaction laser; (iii) a 8 channels direct conversion receiver, which provides the base-band demodulation of the RF signals picked-up along the accelerator (gun probes, directional couplers, etc.). Moreover, the system comprises the low voltage

power supply for the splitting board, and the solid state power amplifier that drives the klystron RF pulse. Each sub-system will be individually characterized in the following paragraphs with particular emphasis to the demodulation board performance evaluation.

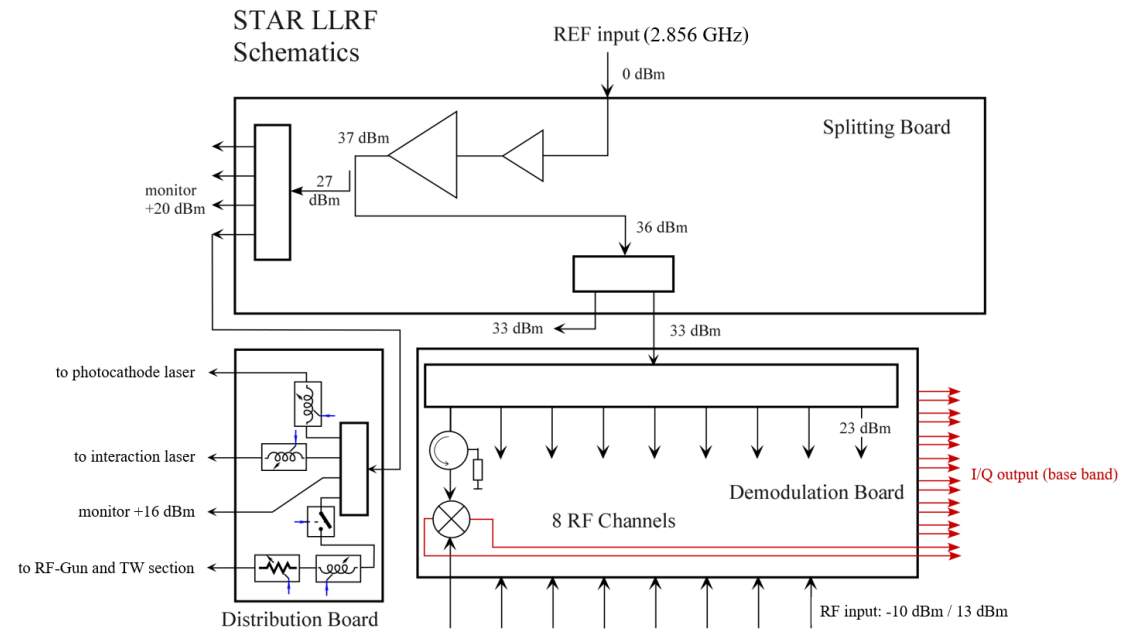


Figure 1: STAR LLRF block diagram. The low voltage power supply for the splitting board and the klystron driver amplifier have not been included.

## 1.1 Splitting board

The splitting board amplifies the RF reference up to the level required by the demodulation board (+33 dBm). In the current implementation only one demodulation board is foreseen, nevertheless the system is ready to support a second unit. A fraction of this signal is spilled by means of a 10 dB directional coupler and is then distributed to the laser clients and the RF power unit. As it can be noted from Figure 1, three additional outputs (+20 dBm) are provided for diagnostics and monitoring purposes. A picture of the assembled splitting board is shown in Figure 2.

## 1.2 Distribution board

The distribution board takes as input one of the 20 dBm monitor outputs of the splitting board, which is further split in four copies. Two are distributed to the laser clients (photocathode and interaction laser), one to the driver amplifier of the RF power station and one has been provided for monitoring purposes. The three copies of the reference which are connected to the lasers and the power unit are equipped with

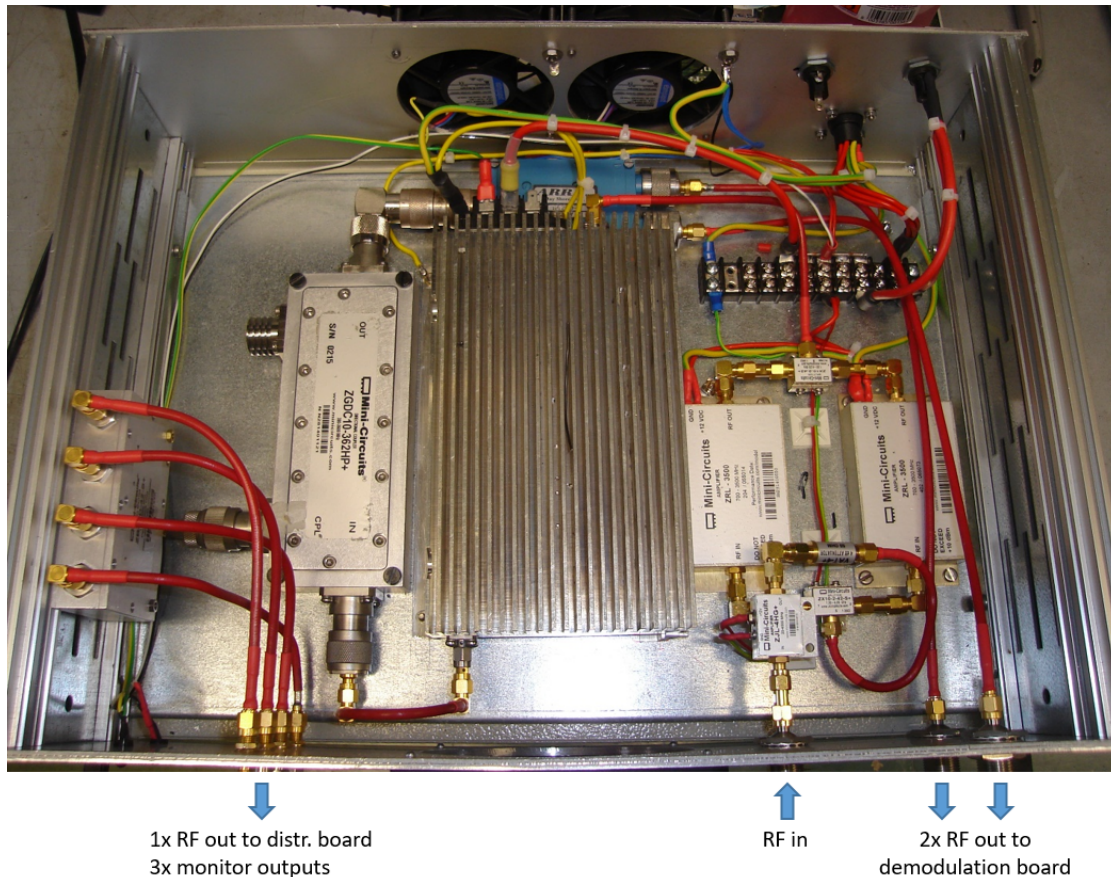


Figure 2: Detail of the splitting board. The RF reference is pre-amplified, split, amplified again and then recombined before entering in the power amplifier stage (covered by cooling fins). Then a fraction of the reference is spilled by a 10 dB directional coupler and is made available for monitoring purposes and for clients. The two copies of the RF reference (33 dBm) are delivered instead to the demodulation board(s).

motor controlled delay lines (ARRA 4428D), but only the one serving the klystron has also an RF switch (Mini-Circuits ZFSWA2-63DR+) and a variable attenuator (Pulsar Microwave AAT-19-479/1S) needed for pulse generation and output level control.

The three lines (n.1 - PC laser, n.2 - interaction laser, n.3 - RF power station) are moved with DC motors driven by variable voltages which are applied by means of three potentiometers. Each delay line has been calibrated as a function of the potentiometer readout and the results, together with the linear fit parameters, are shown in Figure 3, Figure 4 and Figure 5 respectively.

The variable attenuator trims the RF level that has to be amplified by the solid state klystron driver. Its attenuation as a function of the control voltage setpoint and the voltage readout by the IOC has been calibrated and reported in Figure 6 top and bottom respectively. The voltage control of the attenuator can be set between 0 V (min attenuation) and 10 V (max attenuation). For system safety, the circuit that drives

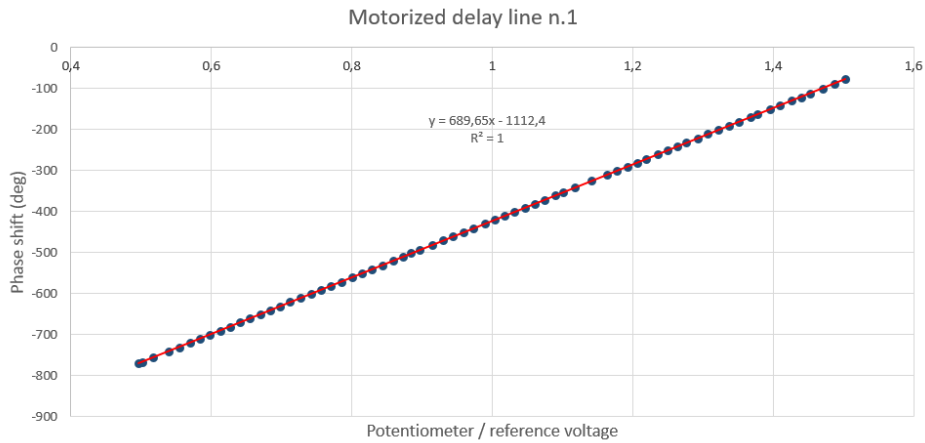


Figure 3: Delay line n.1 calibration: phase shift as a function of the ratio of potentiometer and reference voltage. The linear fitting function is  $y = 689.65x - 1112.4$ .

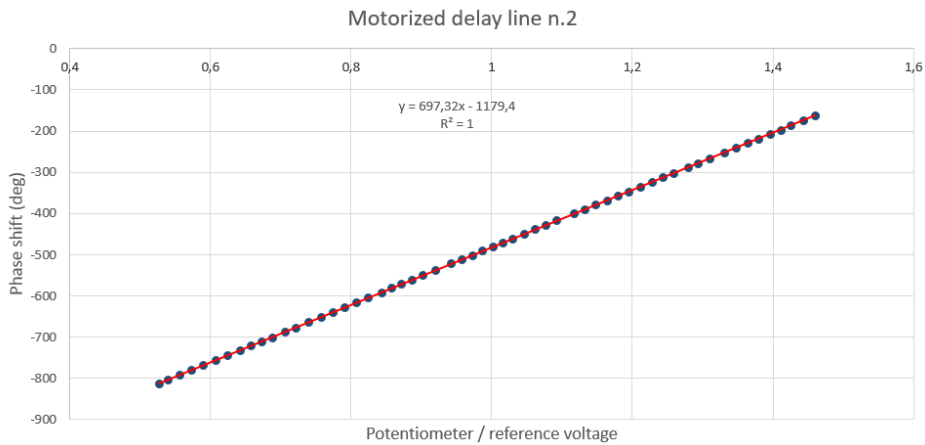


Figure 4: Delay line n.2 calibration: phase shift as a function of the ratio of potentiometer and reference voltage. The linear fitting function is  $y = 697.32x - 1179.4$ .

the attenuator inverts the control logic such that, in case of power supply failure (0 V), the attenuation is set to maximum. This explains the inverted slopes of the attenuation function in the top and bottom plot of Figure 6. Both plots have been fitted to a 4<sup>th</sup> order polynomial function which, as well as the linear fit to the delay lines data, needs to be included in the control system for machine operation. A picture of the distribution board is shown in Figure 7.

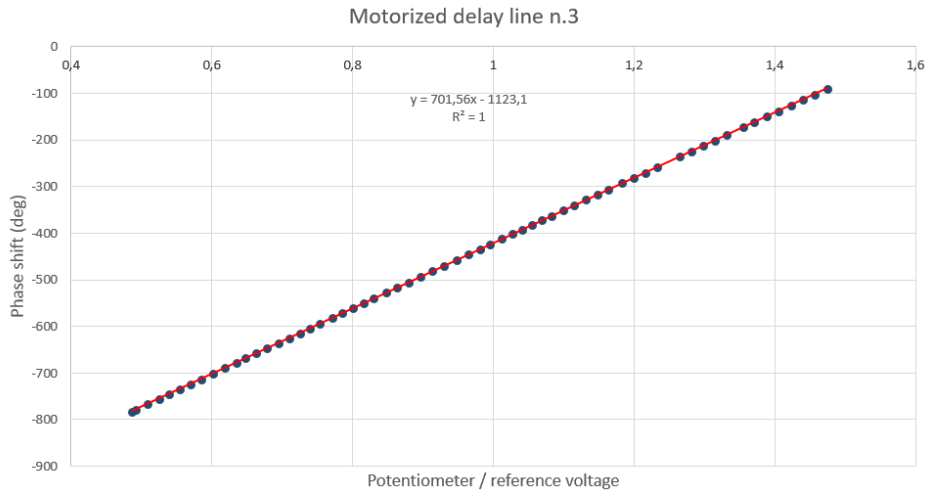


Figure 5: Delay line n.3 calibration: phase shift as a function of the ratio of potentiometer and reference voltage. The linear fitting function is  $y = 701.56x - 1123.1$ .

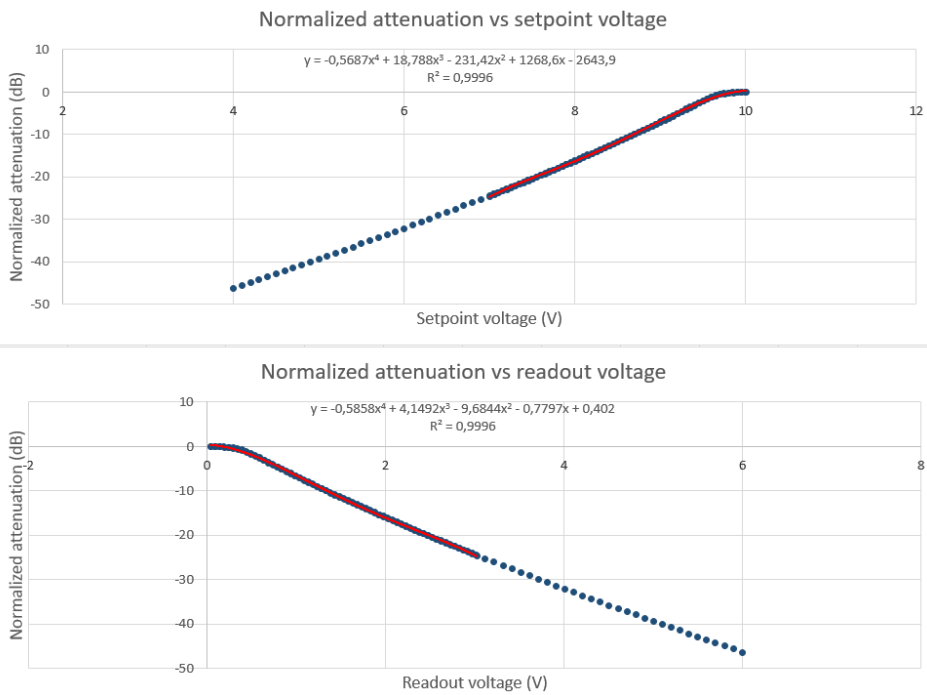


Figure 6: Variable attenuator calibration as a function of the voltage setpoint (top) and the voltage readout (bottom). In both cases the trend has been fitted to a 4<sup>th</sup> order polynomial function, obtaining the functions:  $y = -0.5687x^4 + 18.788x^3 - 231.42x^2 + 1268.6x - 2643.9$  and  $y = -0.5858x^4 + 4.1492x^3 - 9.6844x^2 - 0.7797x + 0.402$  respectively.

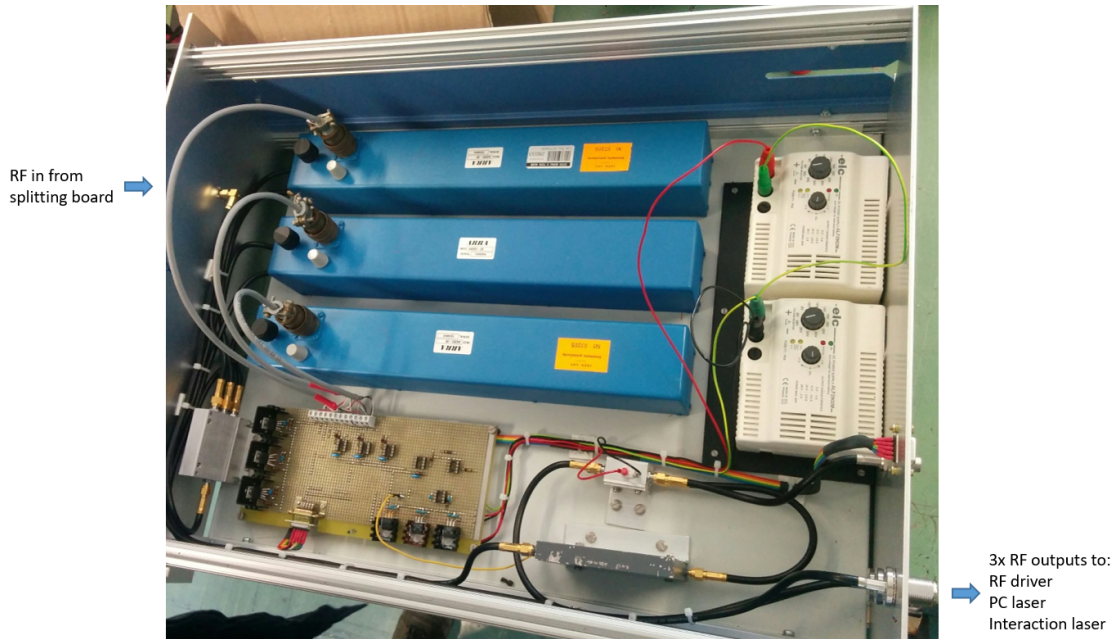


Figure 7: Detail of the distribution board. A 3-way splitter generates the three copies of the RF reference to be delivered to the clients. Each one of these is connected to a variable delay line, and only the one serving the klystron driver has a voltage controlled attenuator and a switch to generate and control the RF pulse.

### 1.3 Demodulation board

The demodulation board working principle is that of a direct conversion receiver, a picture of it is shown in Figure 8. The 33 dBm LO signal (2856 MHz) amplified in the splitting board is delivered to each demodulator channel via a 9 way splitter and an isolator, which protects the splitting board final amplifier from power reflections and provides an optimal isolation of each mixer. After the isolators, I/Q mixers perform the frequency down-conversion to base-band for the 8 channels available. The front panel of the board includes both the 8 RF input connectors (N-type) and the  $2 \times 8$  output I/Q connectors (BNC), while the rear panel hosts only the LO input.

The first step of the demodulator characterization has been the measurement of its fundamental parameters, such as: conversion loss, voltage offset and the phase error between *in phase* (I) and *in quadrature* (Q) signals. The measurement has been carried out feeding to the demodulator a CW RF signal with a 2 kHz frequency shift with respect to the LO ( $f_{RF} = 2855.998$  MHz) and varying the level of the RF input signal between -10 dBm and 15 dBm. For each input level the I/Q output pulses have been acquired with two 8-channels 60 MS/s 12 bit digitizer cards (NI PXI-5105,  $\pm 3$  V dynamic range) and

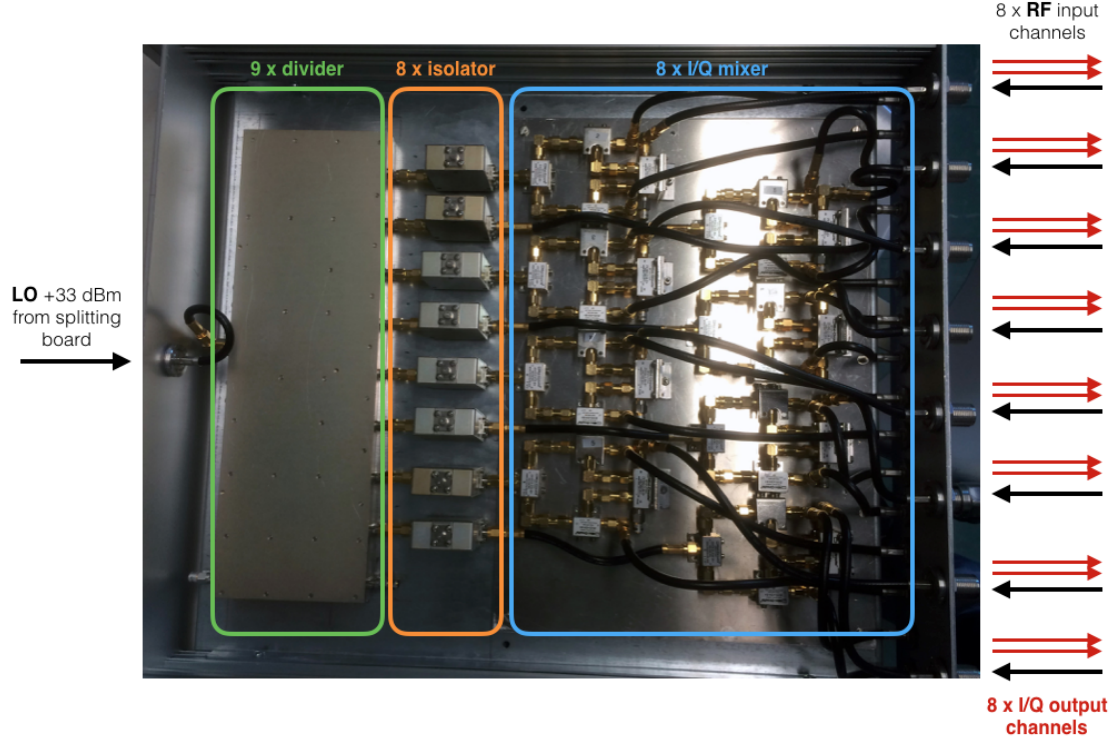


Figure 8: LLRF demodulation board. The LO reference signal (+33 dBm) is split by a 9-way divider (green box), each channel has its own isolator (orange box) to avoid reflections back to the splitting board and an I/Q mixer (blue box). The front panel hosts the 8 N-type input connectors as well as the  $2 \times 8$  BNC output channels.

fitted according to the analytical models reported in equation 1 and 2:

$$I = V_{RF} \cdot k_I \cdot \cos(2\pi f_I t + \phi_I) + V_I \quad (1)$$

$$Q = V_{RF} \cdot k_Q \cdot \sin(2\pi f_Q t + \phi_Q) + V_Q \quad (2)$$

where  $V_{RF}$  is the RF input amplitude (in linear scale),  $k_I$  and  $k_Q$  are the conversion loss factors,  $f_I$  and  $f_Q$  the fitted frequencies of the two pulses ( $f_I \simeq f_Q \simeq f_{LO} - f_{RF}$ ),  $\phi_I$  and  $\phi_Q$  the initial phase values,  $V_I$  and  $V_Q$  the voltage offsets of I and Q pulse respectively. The phase shift between I and Q components has been defined as:

$$\Delta\phi = \phi_Q - \phi_I \quad (3)$$

Conversion loss and voltage offset values have been reported in Figure 9, Figure 10, Figure 11 and Figure 12 for I and Q channels respectively. Finally the phase shift between the two pulses is shown in Figure 13.

Once all the mixers have been characterized, it is useful to explain how voltage offset, conversion

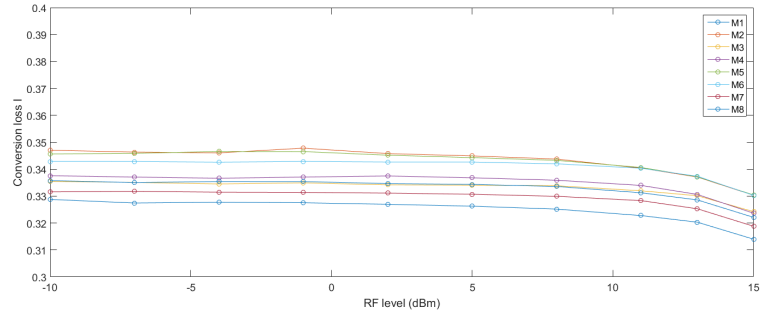


Figure 9: Conversion loss I component ( $k_I$ ) as a function of RF input level.

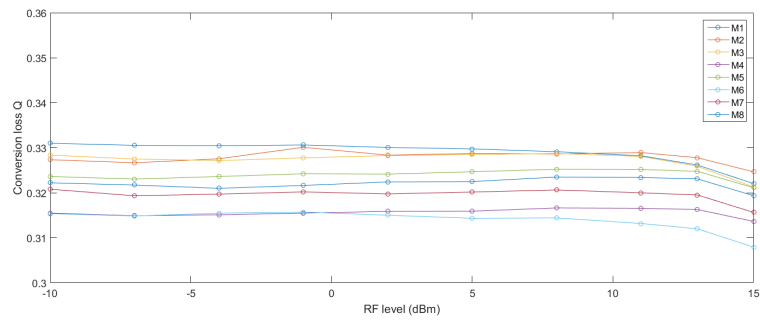


Figure 10: Conversion loss Q component ( $k_Q$ ) as a function of RF input level.

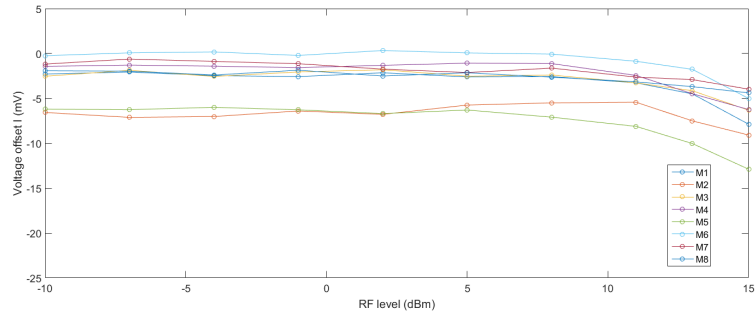


Figure 11: Voltage offset I component ( $V_I$ ) as a function of RF input level.

loss and phase shift can be used to compensate the non-ideality of real, I-Q mixer based, demodulators. Ideally, the I-Q axes are an orthonormal reference frame, where any waveform of amplitude  $V_{RF}$  and phase  $\phi$  can be decomposed in its ideal in-phase and in-quadrature component ( $I_i, Q_i$ ), as shown in Figure 14 (left). Either an imbalance between conversion loss values, or the existence of voltage offsets of I and Q waveforms, or a non perfect orthogonality between I and Q components cause the I-Q reference frame to be non orthonormal and to have a certain offset ( $O_I, O_Q$ ) with respect to the ideal case, as shown

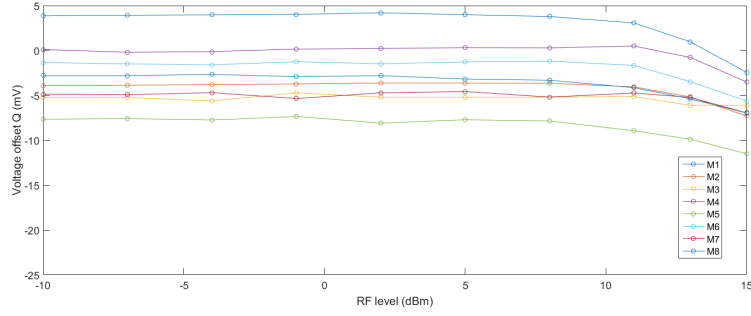


Figure 12: Voltage offset Q component ( $V_Q$ ) as a function of RF input level.

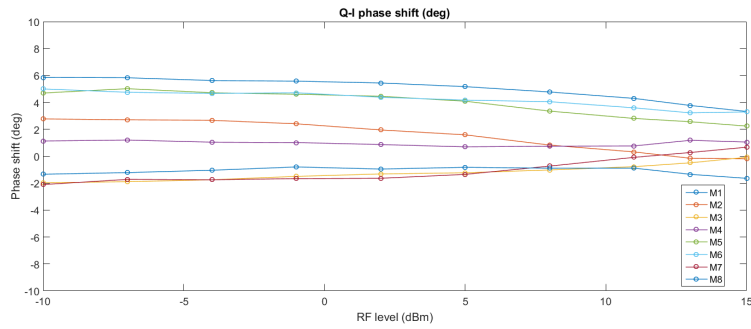


Figure 13: Phase shift ( $\Delta\phi = \phi_Q - \phi_I$ ) as a function of RF input level.

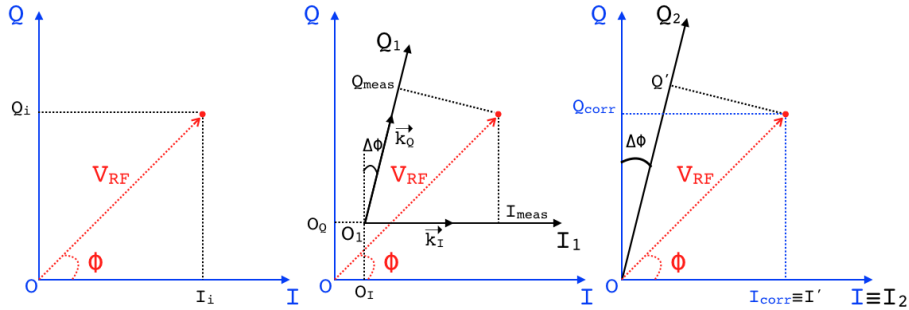


Figure 14: I-Q Cartesian representation. (Left) ideal case: I and Q are an orthonormal base, any signal of amplitude  $V_{RF}$  and phase  $\phi$  can be written as a function of its components  $I_i$  and  $Q_i$ . (Center) real case: the I-Q reference frame has an offset,  $k_I \cdot k_Q \neq 0$  and  $|k_I| \neq |k_Q| \neq 1$ . The two measured components ( $I_{meas}$ ,  $Q_{meas}$ ) cannot be reliably used to represent the original signal and then a correction is needed. (Right) once the measured I-Q have been compensated for voltage offset and conversion loss ( $I'$ ,  $Q'$ ) a further correction, that accounts for  $\Delta\phi \neq 0$ , is necessary to obtain the values  $I_{corr}$ ,  $Q_{corr}$  used to assess the performance of the LLRF system.

in Figure 14 (center). Hence, in order to get an accurate result, any real measurement of I-Q ( $I_{meas}$ ,  $Q_{meas}$ ) has to be compensated for voltage offsets and conversion loss ( $I'$ ,  $Q'$ ) and finally for  $\Delta\phi$ , see

Table 1: Demodulator single channel parameters (average values from fit).

Mixer	$k_I$	$k_Q$	$V_I(mV)$	$V_Q(mV)$	$\Delta\phi$ (rad)
1	0.3247	0.3288	-3.24	2.94	0.087
2	0.3429	0.3279	-6.72	-4.27	0.026
3	0.3328	0.3271	-2.95	-5.38	-0.021
4	0.3347	0.3156	-2.24	-0.30	0.017
5	0.3426	0.3240	-7.59	-8.43	0.067
6	0.3406	0.3138	-0.75	-2.04	0.073
7	0.3290	0.3196	-1.88	-5.12	-0.018
8	0.3326	0.3221	-2.67	-3.70	-0.019

Figure 14 (right), and numerically described in the following equations.

In this framework, two methods have been used in order to estimate the amplitude and phase reconstruction performance of the demodulator. The first corrects the measured I and Q pulses with the average values of the fitted parameters for each channel (which have been summarized in Table 1). In the second method, instead, the correction is done for each input level with the appropriate parameter obtained from the fit (for this reason it will be referred to as “local” in the following).

The raw amplitude and phase values have been defined according to the following relations:

$$A_{meas} = \frac{\sqrt{I^2 + Q^2}}{k_{avg}} \quad (4)$$

$$\Phi_{meas} = \text{atan2}(Q, I) \quad (5)$$

where  $k_{avg}$  is the average value of  $k_I$  and  $k_Q$  and  $\text{atan2}$  is the so called “two arguments arctangent” ( $-\pi < \text{atan2}(y, x) \leq \pi$ ). The errors on the reconstructed amplitude and phase have been defined as:

$$Err A_{meas} = \frac{A_{meas} - V_{RF}}{V_{RF}} \quad (6)$$

$$Err \Phi_{meas} = \Phi_{meas} - \Phi_{real} \quad (7)$$

where  $\Phi_{real}$  is the reference phase, defined as:

$$\Phi_{real} = 2\pi f_{avg}t + \phi_I \quad (8)$$

where  $f_{avg} = (f_I + f_Q)/2$  is the average value of the fitted frequencies  $f_I$  and  $f_Q$  and  $t$  is the time value extracted from the acquired waveform.

The first reconstruction method applies an average correction based on the equations 1 and 2. First of all the amplitudes of I and Q pulses have been compensated with average offsets and conversion losses:

$$I' = \frac{I - \overline{V_I}}{\overline{k_I}} \quad (9)$$

$$Q' = \frac{Q - \overline{V_Q}}{\overline{k_Q}} \quad (10)$$

Then, in order to take into account also the average phase shift error ( $\overline{\Delta\phi}$ ) between I and Q waveforms, the corrected values have been defined:

$$I_{corr} = A_{corr} \cdot \cos(\Phi_{corr}) = I' \quad (11)$$

$$Q_{corr} = A_{corr} \cdot \sin(\Phi_{corr}) = \frac{Q' - I' \sin(\overline{\Delta\phi})}{\cos(\overline{\Delta\phi})} \quad (12)$$

finally the amplitude and phase have been derived:

$$A_{corr} = \sqrt{I_{corr}^2 + Q_{corr}^2} = \sqrt{I'^2 + \left(\frac{Q' - I' \sin(\overline{\Delta\phi})}{\cos(\overline{\Delta\phi})}\right)^2} \quad (13)$$

$$\Phi_{corr} = \text{atan2}(Q_{corr}, I_{corr}) = \text{atan2}\left(Q' - I' \sin(\overline{\Delta\phi}), I' \cos(\overline{\Delta\phi})\right) \quad (14)$$

The definitions of amplitude and phase error are still the ones in equations 6 and 7 substituting  $A_{meas}$  and  $\Phi_{meas}$  with  $A_{corr}$  and  $\Phi_{corr}$ . The results obtained with the average compensation have been shown in Figure 15 and Figure 16 for amplitude and phase respectively. It is evident that the raw correction of amplitude and phase for conversion loss only (black triangles) does not allow an accurate reconstruction of the original signal, for amplitude errors up to 25% and maximum phase errors up to 25° might be achieved. Using the simple average correction method, instead, a maximum of 5% rms amplitude and 4° rms phase error has been obtained.

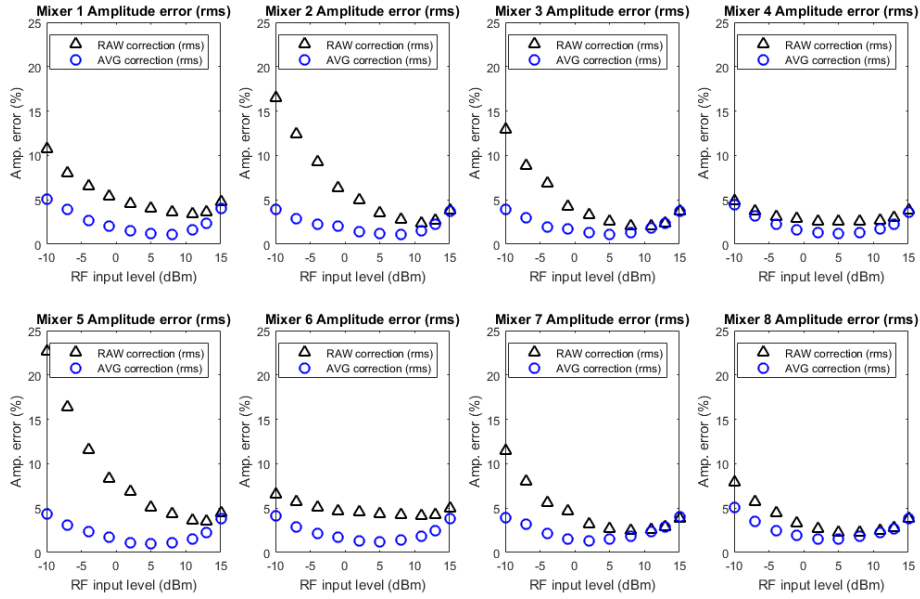


Figure 15: Amplitude error comparison: Raw correction (black) and average correction (blue) rms values.

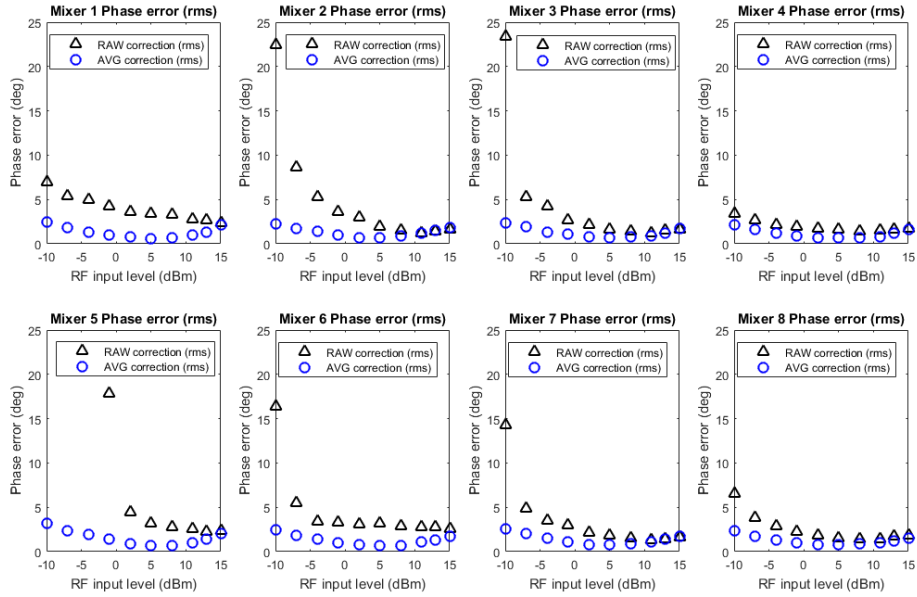


Figure 16: Phase error comparison: Raw correction (black) and average correction (blue) rms values.

The second approach to improve the pulse reconstruction performance makes use of “local” values instead of averages. This could be of particular interest especially when the unknown RF signal level is lower than 0 dBm, as the impact of the voltage offset correction becomes more significant. Then, all the average parameters in equation 9, 10, 11, 12, 13, 14 must be substituted with their “local” values. Unfortunately, this second correction scheme requires for each channel and for each RF pulse a raw amplitude and phase reconstruction, in order to interpolate the most appropriate value of each parameter in a look up table, and only then the refined amplitude and phase can be computed. Depending on control system architecture, cpu power available and the maximum error sustainable one can choose the most suitable reconstruction scheme.

The comparison between the two correction methods proposed in this note is shown in Figure 17 for the amplitude and in Figure 18 for the phase, while the performances of each mixer have been listed in Appendix A. As anticipated, the impact of the local method can be appreciated either when the voltage offsets represent a non negligible fraction of the RF input level ( $< 0$  dBm), or when mixer saturation comes into play ( $> 10$  dBm). In general, applying the local correction scheme allows to have a more uniform behaviour of each mixer, compensating at best each non-ideality. However, as it can be noted from Figure 17 and Figure 18, the local correction does not result in a dramatic improvement in the reconstruction accuracy. It has been noted, in fact, that for low input levels the correction suffers from the limited vertical resolution of the digitizer (which has been fixed to  $\pm 3$  V during the calibration).

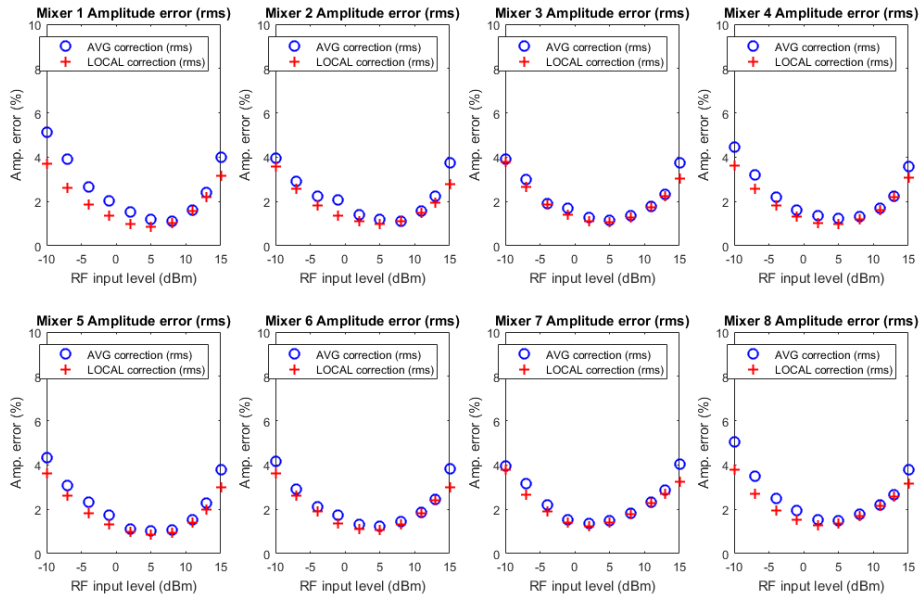


Figure 17: Amplitude error comparison: average (blue) and local (red) correction RMS values.

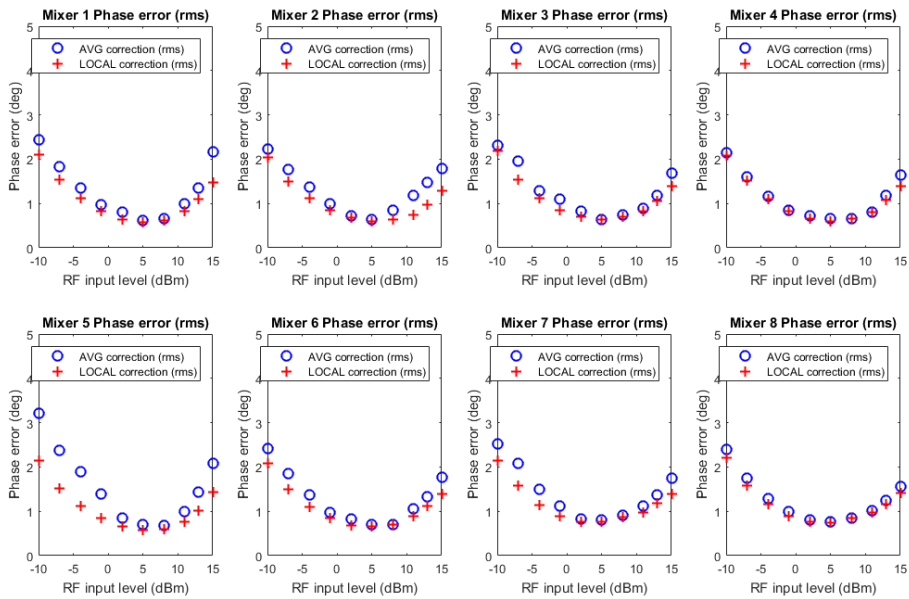


Figure 18: Phase error comparison: average (blue) and local (red) correction RMS values.

This is shown in Figure 19 for mixer 1 at -7 dBm, where the vertical sampling of the input waveform (red circles) is somewhat evident. The fit to the waveform (blue line) is then performed on an *artificially jittering* signal, that limits the amplitude and phase resolution achievable. This effect could be reduced setting the digitizer vertical resolution on a smaller scale (e.g.  $\pm 0.5$  V).

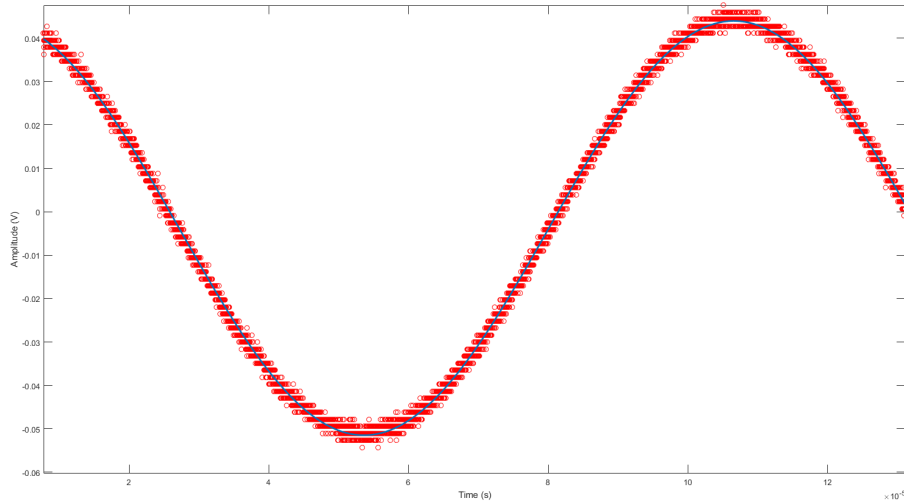


Figure 19: Mixer 1 output waveform (red) acquired with an RF input level of -7 dBm and its relative fit (blue). The effect of the limited vertical resolution ( $\pm 3$  V, 12 bits) is evident, this corresponds to an artificial amplitude and phase jitter that deteriorates the performance of the correction method.

Hence, the best choice between accuracy and implementation simplicity appears to be the use of the average correction. In fact, if the RF level is kept within 0 dBm and 10 dBm, both methods allow to reach a precision lower than 2% and  $1^\circ$  on the reconstructed amplitude and phase respectively.

## Appendix A - Single channel amplitude and phase errors

Table 2: Errors mixer 1.

Level IN (dBm)	Err <sub>A</sub> avg (%)	Err <sub>A</sub> loc (%)	Err <sub>φ</sub> avg (deg)	Err <sub>φ</sub> loc (deg)
-10	5.1	3.7	2.4	2.1
-7	3.9	2.6	1.8	1.5
-4	2.7	1.9	1.3	1.1
-1	2.0	1.3	1.0	0.8
2	1.5	1.0	0.8	0.6
5	1.2	0.9	0.6	0.6
8	1.1	1.0	0.6	0.6
11	1.6	1.6	1.0	0.8
13	2.4	2.2	1.4	1.1
15	4.0	3.2	2.2	1.5

Table 3: Errors mixer 2.

Level IN (dBm)	Err <sub>A</sub> avg (%)	Err <sub>A</sub> loc (%)	Err <sub>φ</sub> avg (deg)	Err <sub>φ</sub> loc (deg)
-10	4.0	3.6	2.2	2.0
-7	2.9	2.6	1.8	1.5
-4	2.2	1.8	1.4	1.1
-1	2.1	1.4	1.0	0.8
2	1.4	1.1	0.7	0.7
5	1.2	1.0	0.6	0.6
8	1.1	1.1	0.8	0.6
11	1.5	1.5	1.2	0.7
13	2.2	2.0	1.5	1.0
15	3.8	2.8	1.8	1.3

Table 4: Errors mixer 3.

Level IN (dBm)	Err <sub>A</sub> avg (%)	Err <sub>A</sub> loc (%)	Err <sub>φ</sub> avg (deg)	Err <sub>φ</sub> loc (deg)
-10	3.9	3.8	2.3	2.2
-7	3.0	2.7	2.0	1.5
-4	1.9	1.9	1.3	1.1
-1	1.7	1.4	1.1	0.9
2	1.3	1.1	0.8	0.7
5	1.1	1.1	0.6	0.6
8	1.3	1.3	0.7	0.7
11	1.8	1.7	0.9	0.8
13	2.3	2.3	1.2	1.1
15	3.8	3.0	1.7	1.4

Table 5: Errors mixer 4.

Level IN (dBm)	Err <sub>A</sub> avg (%)	Err <sub>A</sub> loc (%)	Err <sub>φ</sub> avg (deg)	Err <sub>φ</sub> loc (deg)
-10	4.5	3.6	2.2	2.1
-7	3.2	2.6	1.6	1.5
-4	2.2	1.8	1.2	1.1
-1	1.6	1.3	0.9	0.8
2	1.4	1.0	0.7	0.7
5	1.2	1.0	0.7	0.6
8	1.3	1.2	0.7	0.6
11	1.7	1.6	0.8	0.8
13	2.2	2.2	1.2	1.1
15	3.6	3.1	1.7	1.4

Table 6: Errors mixer 5.

Level IN (dBm)	Err <sub>A</sub> avg (%)	Err <sub>A</sub> loc (%)	Err <sub>φ</sub> avg (deg)	Err <sub>φ</sub> loc (deg)
-10	4.3	3.6	3.2	2.2
-7	3.1	2.6	2.4	1.5
-4	2.3	1.8	1.9	1.1
-1	1.8	1.3	1.4	0.8
2	1.1	1.0	0.9	0.6
5	1.0	0.9	0.7	0.6
8	1.1	0.9	0.7	0.6
11	1.5	1.4	1.0	0.8
13	2.3	2.0	1.4	1.0
15	3.8	3.0	2.1	1.4

Table 7: Errors mixer 6.

Level IN (dBm)	Err <sub>A</sub> avg (%)	Err <sub>A</sub> loc (%)	Err <sub>φ</sub> avg (deg)	Err <sub>φ</sub> loc (deg)
-10	4.2	3.6	2.4	2.1
-7	2.9	2.6	1.8	1.5
-4	2.1	1.9	1.4	1.1
-1	1.7	1.3	1.0	0.8
2	1.3	1.1	0.8	0.7
5	1.2	1.1	0.7	0.7
8	1.4	1.3	0.7	0.7
11	1.9	1.8	1.0	0.9
13	2.5	2.4	1.3	1.1
15	3.8	3.0	1.8	1.4

Table 8: Errors mixer 7.

Level IN (dBm)	Err <sub>A</sub> avg (%)	Err <sub>A</sub> loc (%)	Err <sub>ϕ</sub> avg (deg)	Err <sub>ϕ</sub> loc (deg)
-10	3.9	3.8	2.5	2.1
-7	3.2	2.6	2.1	1.6
-4	2.2	1.9	1.5	1.1
-1	1.5	1.4	1.1	0.9
2	1.3	1.3	0.8	0.8
5	1.5	1.4	0.8	0.8
8	1.8	1.8	0.9	0.9
11	2.3	2.3	1.1	1.0
13	2.9	2.7	1.4	1.2
15	4.0	3.2	1.7	1.4

Table 9: Errors mixer 8.

Level IN (dBm)	Err <sub>A</sub> avg (%)	Err <sub>A</sub> loc (%)	Err <sub>ϕ</sub> avg (deg)	Err <sub>ϕ</sub> loc (deg)
-10	5.0	3.8	2.4	2.2
-7	3.5	2.7	1.7	1.6
-4	2.5	2.0	1.3	1.2
-1	1.9	1.5	1.0	0.9
2	1.5	1.3	0.8	0.8
5	1.5	1.4	0.8	0.7
8	1.8	1.7	0.8	0.8
11	2.2	2.2	1.0	1.0
13	2.7	2.6	1.2	1.2
15	3.8	3.2	1.6	1.4

## References

- [1] K. Dobashi, *et al.*, Development of compact hard X-ray source based on laser-electron collision using X-band linac, in: Proceedings of EPAC 2002, Paris, France.
- [2] A. Jochmann, *et al.*, Phys. Rev. Lett. **111**, 114803 (2013).
- [3] M. Babzien, *et al.*, Phys. Rev. Lett. **96**, 054802 (2006).
- [4] L. Serafini and J. Rosenzweig, Phys. Rev. E **55**, 7565 (1997).
- [5] M. Ferrario, *et al.*, Phys. Rev. Lett. **99**, 234801 (2007).
- [6] M. Ferrario, *et al.*, Phys. Rev. Lett. **104**, 054801 (2010).